Effect of disorder on the dilute equilibrium vacancy concentrations of multicomponent crystalline solids

Anna A. Belak and Anton Van der Ven

Phys. Rev. B **91**, 224109 — Published 24 June 2015

DOI: 10.1103/PhysRevB.91.224109

The effect of disorder on the dilute equilibrium vacancy concentrations of multi-component crystalline solids

Anna A. Belak
Department of Materials Science and Engineering, University of Michigan, Ann Arbor, MI 48109

Anton Van der Ven*
Materials Department, University of California Santa Barbara, Santa Barbara, CA 93106,
Department of Materials Science and Engineering, University of Michigan, Ann Arbor, MI 48109

We develop statistical mechanical methods to predict the thermodynamic properties of dilute vacancies in multi-component solids from first principles. The approach relies on a coarse graining procedure to predict dilute vacancy concentrations with Monte Carlo simulations in alloys exhibiting varying degrees of short and long-range order. We apply this approach to a study of vacancies in hcp based Ti-Al binary alloys and find a strong dependence of the equilibrium vacancy concentration on the Al concentration and the degree of long-range order, especially at low temperature.

PACS numbers: 61.72.Bb, 61.66.Dk, 82.60.Lf

I. INTRODUCTION

All crystalline solids contain imperfections, the most common of which are vacancy and interstitial point defects. Their thermodynamic origin is often entropic as defect formation energies tend to be positive. While the nature of point defects in single component solids or highly ordered compounds has received much experimental and theoretical attention[1–8], far less effort has been devoted to understanding the nature and concentration dependence of point defects in disordered multi-component solids or ordered compounds that can tolerate a high degree of off-stoichiometry. Almost all metals used in structural applications are alloys containing a variety of elements that are added to optimize a mix of mechanical, kinetic and phase stability related properties[9,10]. Alloys of semiconducting compounds are increasingly utilized in electronic applications and are also actively pursued in thermoelectrics as a way to reduce thermal conductivity[11–14]. Changing the overall concentration of an alloy should affect the equilibrium point defect concentration, as point defects will interact differently with the various components of the solid. Furthermore, point defect concentrations are likely to depend on the degree of short and long-range order, which itself is a function of temperature and overall concentration. In ordered compounds, point defects play a crucial role in accommodating off-stoichiometry, with some intermetallic compounds having sublattice vacancy concentrations that can reach several percent[15].

Even low concentrations of point defects can have a dramatic effect on a range of properties that include electronic and atomic mobilities. Vacancies, interstitials, and more complex anti-site or dumbbell-like defects scatter Bloch states thereby resulting in lower electronic conductivity. In semiconductors, they can also alter the Fermi level and thereby modify the number of free carriers, either by trapping them or donating them to the conduction band. Point defects are especially important in mediating atomic transport within the crystalline state. Interstitial point defects are typically more mobile[16–20], but vacancies are essential to redistribute substitutional elements within alloys[21]. The Kirkendall effect is among the most pronounced manifestations of vacancy mediated substitutional diffusion within alloys and arises due to a difference in vacancy exchange frequencies among the various components of the alloy[21–24]. Any concentration gradient in such alloys results in a net vacancy flux in a direction opposite to the flux of the fastest diffuser. In the presence of vacancy sources and sinks such as dislocations and grain boundaries, a net vacancy flux results in a rigid drift of the crystal frame of reference, often causing deleterious effects within the solid, such as void formation.

Substitutional diffusion coefficients are to first order proportional to the vacancy concentration[21]. Variations in alloy concentration or the degree of short or long-range order will affect the vacancy concentration and thereby the mobility of the constituents of the alloy. There is limited understanding of the dependence of the equilibrium vacancy concentration on alloy concentration and degree of order due to difficulties in directly and precisely measuring vacancy concentrations in multi-component solids. Such understanding is crucial in high temperature applications relying on heterostructures with strong built in chemical potential gradients that drive interdiffusion[24,25]. It is also of importance in thermoelectric applications where temperature gradients can result in driving forces for demixing, which can be enhanced by high concentrations of point defects.

Here, we develop statistical mechanical methods to predict the thermodynamic properties of dilute vacancies within multi-component solids from first principles. We introduce a coarse graining procedure that enables the prediction of very dilute vacancy concentrations and their associated thermodynamic properties with Monte Carlo simulations. When applied to hcp based Ti-Al binary alloys, we find a strong dependence of the equilibrium

vacancy concentration on Al concentration and degree of long-range order, especially at low temperature.

II. METHODS

A. Alloy Hamiltonian and vacancies

As an alloy Hamiltonian, we use a cluster expansion, which is a mathematical tool to describe any property of a multi-component crystalline solid that depends on how the various components of the solid are arranged within a particular parent crystal structure[26,27]. It relies on occupation variables assigned to each site within a crystal that can take on discrete values depending on the specie occupying the site. In a binary A-B alloy, spin-like occupation variables, σ_i, are typically used, which take a value of $+1$ if site i in the crystal is occupied by B and -1 if it is occupied by A. Polynomials constructed by taking products of occupation variables belonging to all possible clusters of sites, including clusters containing only one site (a point cluster), pair clusters, triplet clusters, etc., can then be shown to form a complete and orthonormal basis in configuration space[26]. Hence, any property of the crystal that depends on how the A and B atoms are arranged on the crystal can be expanded in terms of these polynomial basis functions. The fully relaxed energy of the crystal, for example, can be written as

$$E\left(\vec{\sigma}\right) \;=\; V_0 + \sum_{\alpha} V_\alpha \cdot \Phi_\alpha\left(\vec{\sigma}\right), \tag{1}$$

where $\vec{\sigma} = \{\sigma_1, ..., \sigma_i, ..., \sigma_M\}$ denotes the collection of all occupation variables in the crystal having M sites, V_0 and V_α are expansion coefficients to be parameterized with a first-principles total energy method, and

$$\Phi_\alpha\left(\vec{\sigma}\right) \;=\; \prod_{i \in \alpha} \sigma_i \tag{2}$$

are cluster functions defined as the product of occupation variables of sites belonging to a cluster of crystal sites α.

The constant term, V_0 in Eq. 1 is equal to the average energy of the crystal in the fully disordered state when there are an equal number of A and B atoms. In the fully disordered state at an alloy concentration $x = 1/2$, the averages of all the cluster functions are zero because the occupation variables of different sites are uncorrelated and the averages of the spin-like occupation variables at $x = 1/2$ are zero. The above expression for the configurational energy of the crystal can thus be viewed as an expansion around the fully disordered alloy at $x = 1/2$. This feature is a result of the particular choice of values that the occupation variables σ_i can take.

Alternative choices for the values of the occupation variables are possible[28,29] and may be more convenient for particular applications. Most metallic alloys and multi-component ceramics of technological importance have a solvent, which is the dominant specie, and a variety of solutes that have significantly lower concentrations than the solvent. Important examples include alloyed steels, which are Fe rich, and Ni-based super-alloys, which are Ni rich. Especially the vacancies within a substitutional alloy, which need to be treated as an explicit component, will have very low concentrations. For these cases, it is more convenient to use an array of occupation variables p_i^B assigned to each site, which are 1 if site i is occupied by specie B and zero otherwise. For an n-component solid, $n-1$ such occupation variables must be assigned to each site. These occupation variables are linearly related to the spin like occupation variables σ_i[30]. While there is no restriction on the choice of $n-1$ occupation variables to explicitly work with, it is most convenient to introduce occupation variables for the solutes only. For a binary A-B alloy also containing vacancies (where A is the solvent) , we would then use p_i^B and p_i^{Va} corresponding to the occupation variables for the solute B and the vacancy 'Va'. In terms of these occupation variables, the total energy of the crystal can be written as

$$E\left(\vec{p}\right) = E_0 + \sum_{\alpha} E_\alpha^{\vec{D}} \cdot \Lambda_\alpha^{\vec{D}}\left(\vec{p}\right), \tag{3}$$

where $\vec{p} = \left\{p_1^B, ..., p_i^B, ..., p_M^B, p_1^{Va}, ..., p_i^{Va}, ..., p_M^{Va}\right\}$ is the collection of all occupation variables for each crystallographic site, and E_0 and $E_\alpha^{\vec{D}}$ are expansion coefficients, again to be determined with a first-principles total energy method. The basis functions are products of occupation variables belonging to the sites of a cluster α and can be written as

$$\Lambda_\alpha^{\vec{D}}\left(\vec{p}\right) = \prod_{i \in \alpha} p_i^{D(i)}. \tag{4}$$

In this expression, the index i runs over the sites of a cluster α while $\vec{D} = \{D(i)\}$ labels the type of occupation variable at each site i (i.e. p_i^B or p_i^{Va}). All cluster basis functions that can be mapped onto each other by a space group symmetry operation of the crystal will have the same expansion coefficient $E_\alpha^{\vec{D}}$. In contrast to a cluster expansion expressed in terms of spin-like occupation variabes, σ_i, the constant term, E_0, in Eq. 3, is now the energy of the pure solvent, as then all of the occupation variables are equal to zero. The above expression can therefore be viewed as an expansion relative to the energy of the crystal containing only solvent atoms A. Hence, for solvent rich alloys we can expect the above expression to converge more rapidly than an equivalent expansion in terms of spin occupation variables. In this work, we develop a multi-component cluster expansion using occupation variables p_i^B and p_i^{Va} (as opposed to spin occupation variables) to describe the configurational energy of a multi-component solid containing a dilute concentration of vacancies. This contrasts with a local cluster expansion approach to treat vacancies in a binary alloy when

using spin-like occupation variables[15,31].

B. Thermodynamics of a binary alloy containing vacancies

Most alloys of technological interest contain dislocations and grain boundaries that act as local vacancy sources and sinks. These extended defects can regulate an equilibrium vacancy concentration within the crystalline regions of the alloy. While a binary substitutional solid contains two atomic species with the amounts of A and B controlled experimentally, in the crystalline regions away from dislocations and grain boundaries, the solid is effectively a ternary system as the number of crystal sites there is conserved and each site can be occupied by A, B or a vacancy. We denote the Gibbs free energy of a crystalline region of M sites that does not include dislocations or grain boundaries with G. Its differential form at constant temperature T and pressure P can be written as

$$dG = \mu_A dN_A + \mu_B dN_B + \mu_{\mathrm{Va}} dN_{\mathrm{Va}},$$

where the μ_i are the chemical potentials of component i and the N_i refer to the number of each component i. This free energy can be normalized by M to yield the Gibbs free energy per crystal site $g = G/M$. The chemical potential of component i, formally defined as

$$\mu_i = \left(\frac{\partial G}{\partial N_i}\right)_{T,P,N_{j\neq i}} \tag{5}$$

can be expressed in terms of g according to[32]

$$\mu_i = g + (\delta_{i,B} - x_B)\frac{\partial g}{\partial x_B} + (\delta_{i,\mathrm{Va}} - x_{\mathrm{Va}})\frac{\partial g}{\partial x_{\mathrm{Va}}} \tag{6}$$

where $\delta_{i,j}$ is the Kronecker delta and the $x_i = N_i/M$ are mole fractions. Due to the conservation of crystal sites in single crystalline regions $x_A + x_B + x_{\mathrm{Va}} = 1$ and only two of the three mole fractions are independent. Graphically, the chemical potentials, μ_i, correspond to the intercept of the plane tangent to the Gibbs free energy $g(x_B, x_{Va})$ with the $x_i = 1$ axis as illustrated in Figure 1.

In the presence of vacancy sources and sinks, the vacancy concentration within crystalline regions cannot be controlled experimentally and is an internal degree of freedom. The solid will then pick the equilibrium vacancy concentration that minimizes the Gibbs free energy at constant T, P, N_A, and N_B. Mathematically this is equivalent to setting the vacancy chemical potential equal to zero

$$\mu_{\mathrm{Va}} = \left(\frac{\partial G}{\partial N_{\mathrm{Va}}}\right)_{T,P,N_A,N_B} = 0. \tag{7}$$

Any deviations in the local vacancy concentration from its equilibrium value will result in a vacancy chemical potential that differs from zero. Using Eq. 6, the vacancy chemical potential can be written in terms of the free energy per crystal site g as

$$\mu_{\mathrm{Va}} = g(x_B, x_{\mathrm{Va}}) - x_B\frac{\partial g}{\partial x_B} + (1 - x_{\mathrm{Va}})\frac{\partial g}{\partial x_{\mathrm{Va}}}, \tag{8}$$

Once the Gibbs free energy per crystal site, $g(x_B, x_{Va})$, is known, it is possible to determine the equilibrium vacancy concentration as a function of the alloy concentration x_B by setting Eq. 8 equal to zero and solving for x_{Va}. This is shown graphically in Figure 1.

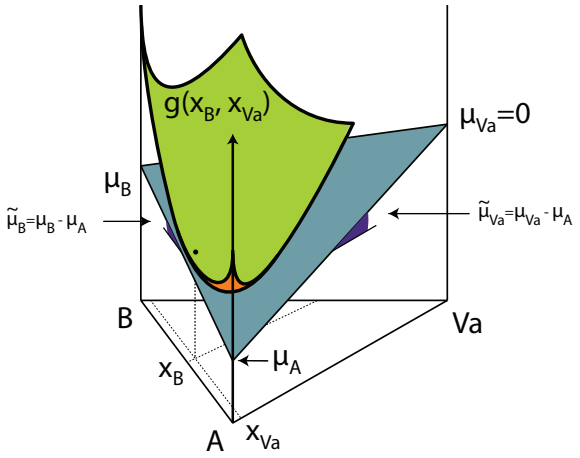

FIG. 1: Ternary free energy diagram with a schematic of the chemical potentials and the zero vacancy chemical potential.

The thermodynamic quantities introduced so far can be calculated with results from semi-grand canonical Monte Carlo simulations. The number of crystal sites, M, remains fixed in a lattice Monte Carlo simulation. Hence, the number of atoms of each component are not independent due to the constraint that $N_A + N_B + N_{\mathrm{Va}} = M$. Since A is the solvent, it is convenient to explicitly track N_B and N_{Va}. Then using $dN_A = dM - dN_B - dN_{\mathrm{Va}}$, the differential of the Gibbs free energy can be rewritten as

$$dG = \tilde{\mu}_B dN_B + \tilde{\mu}_{\mathrm{Va}} dN_{\mathrm{Va}} + \mu_A dM. \tag{9}$$

with the exchange chemical potentials defined as $\tilde{\mu}_B = \mu_B - \mu_A$ and $\tilde{\mu}_{\mathrm{Va}} = \mu_{\mathrm{Va}} - \mu_A$. At constant M (i.e. $dM = 0$), the exhange chemical potentials, $\tilde{\mu}_B$ and $\tilde{\mu}_{\mathrm{Va}}$ are conjugate to N_B and N_{Va} respectively. Eq. 9 also shows that the exchange chemical potentials, $\tilde{\mu}_B$ and $\tilde{\mu}_{\mathrm{Va}}$, are related to the Gibbs free energy per crystal site $g = G/M$ according to

$$\tilde{\mu}_B = \frac{\partial g}{\partial x_B} \qquad \tilde{\mu}_{\mathrm{Va}} = \frac{\partial g}{\partial x_{\mathrm{Va}}} \tag{10}$$

These relations suggest that it is natural to work within the semi-grand canonical ensemble in which $\tilde{\mu}_B$ and $\tilde{\mu}_{\mathrm{Va}}$ are controlled at constant temperature. The partition

function within this semi-grand canonical ensemble when considering only configurational excitations can be written as

$$Z = \sum_{\vec{p}} e^{-\beta\Omega(\vec{p})}, \tag{11}$$

where $\beta = 1/kT$ and k is the Boltzmann constant. The semi-grand canonical energy, $\Omega(\vec{p})$, appearing in Eq. 11 is defined as

$$\Omega\left(\vec{p}\right) = E\left(\vec{p}\right) - N_B\tilde{\mu}_B - N_{\mathrm{Va}}\tilde{\mu}_{\mathrm{Va}} \tag{12}$$

with $E\left(\vec{p}\right)$ the energy of configuration $\vec{p}$.

Semi-grand canonical Monte Carlo simulations of a crystal containing A, B and vacancies enable the calculation of ensemble averages of the semi-grand canonical energy Ω and the averages of the number of B and vacancies, N_B and N_{Va}, all as a function of temperature, T, and exchange chemical potentials, $\tilde{\mu}_B$ and $\tilde{\mu}_{\mathrm{Va}}$. The free energy per crystal site at constant temperature, $g(x_B, x_{\mathrm{Va}})$, can then be calculated by integrating Eq. 10 along a path for which $x_B = N_B/M$ and $x_{\mathrm{Va}} = N_{\mathrm{Va}}/M$ has been calculated as a function of $\tilde{\mu}_B$ and $\tilde{\mu}_{\mathrm{Va}}$. More details about free energy integration methods can be found for example in References[15,33].

A simplification in the determination of the equilibrium vacancy concentration is possible for substitutional alloys having very dilute equilibrium vacancy concentrations. Combining Eq. 8 and Eq. 10 we can solve for $\tilde{\mu}_{\mathrm{Va}}$ as a function of $\tilde{\mu}_B$ along the path corresponding to an equilibrium vacancy concentration (i.e. $\mu_{\mathrm{Va}} = 0$)

$$\tilde{\mu}_{\mathrm{Va}} = -\frac{g\left(x_B, x_{\mathrm{Va}}\right) - x_B\tilde{\mu}_B}{\left(1 - x_{\mathrm{Va}}\right)}. \tag{13}$$

When the equilibrium vacancy concentration is very dilute, we can accurately approximate the free energy per crystal site, $g(x_B, x_{\mathrm{Va}})$, with that of the strict binary, $g(x_B, x_{\mathrm{Va}} = 0)$. Furthermore, $1 - x_{\mathrm{Va}}$ can be approximated as 1. The resulting expression then allows us to determine a path in $\tilde{\mu}_{\mathrm{Va}}$ and $\tilde{\mu}_B$ space corresponding to an equilibrium vacancy concentration with knowledge only of the binary free energy $g(x_B, x_{\mathrm{Va}} = 0)$. The resulting values of $\tilde{\mu}_{\mathrm{Va}}$ and $\tilde{\mu}_B$ can then be used as input for semi-grand canonical Monte Carlo simulations of the ternary alloy (A, B and vacancies) to calculate the equilibrium vacancy concentration as a function of alloy concentration x_B.

C. Coarse graining the vacancies in an alloy partition function

The equilibrium vacancy concentrations on the substitutional sites of many alloys are exceedingly low. The vacancy formation energy in hcp Ti as predicted with approximations to DFT, for example, are in the vicinity of 2 eV[34,35]. Effective vacancy formation energies of 1.55±0.2 eV and 1.8±0.2 eV have been reported in ordered Ti_3Al at off-stoichiometric concentrations as determined with positron lifetime measurements[36]. A large fraction of substitutional binary alloys and multi-component solids contain thermal vacancies, which are usually substantially more dilute than structural vacancies that accommodate off-stoichiometry as occurs in some intermetallic compounds such as Al rich B2-NiAl[15]. Calculating the equilibrium vacancy concentration in binary alloys when their concentrations are very low using a cluster expansion and Monte Carlo simulations requires a very large number of Monte Carlo passes[31]. An equilibrium vacancy concentration of 10^{-12} in an fcc or hcp based alloy, for example, will require on average 10^9 Monte Carlo passes in a $10 \times 10 \times 10$ Monte Carlo cell to sample the occurrence of a single vacancy. The statistics using traditional Metropolis Monte Carlo will therefore be poor and will require exorbitant simulation times. Since the occurrence of vacancies at these equilibrium vacancy concentrations is so rare, though, it becomes feasible and sufficiently accurate to perform a coarse graining procedure combined with a low-temperature-like expansion of the partition function.

Configurations with vacancies in alloys where the equilibrium vacancy concentration is very low, have much higher grand canonical energies than configurations without vacancies, and therefore have a much lower probability of occurrence compared to purely binary A-B configurations. We can use this fact to develop a coarse graining scheme valid for a grand canonical Monte Carlo simulation of a crystal having periodic boundary conditions. We proceed by writing the sum over all configurations $\vec{p}$ as first a sum over binary configurations $\vec{s}$ followed by a sum over all configurations obtained by inserting vacancies into the binary A-B configuration $\vec{s}$, which we denote by $\vec{q}(\vec{s})$. To avoid double counting of configurations containing vacancies, we only sum over vacancy configurations $\vec{q}(\vec{s})$ obtained from $\vec{s}$ by exchanging either A or B with a vacancy, but not both.

$$Z = \sum_{\vec{s}} \left\{ e^{-\beta\Omega(\vec{s})} + \sum_{\vec{q}(\vec{s})} e^{-\beta\Omega(\vec{q}(\vec{s}))} \right\} \tag{14}$$

$$Z = \sum_{\vec{s}} e^{-\beta\Omega(\vec{s})} \left\{ 1 + \sum_{\vec{q}(\vec{s})} e^{-\beta\Delta\Omega(\vec{q}(\vec{s}))} \right\} \tag{15}$$

with

$$\Delta\Omega\left(\vec{q}(\vec{s})\right) = \Omega\left(\vec{q}(\vec{s})\right) - \Omega\left(\vec{s}\right) \tag{16}$$

equal to the cost in the grand canonical energy of introducing vacancies having configuration $\vec{q}(\vec{s})$ derived from a binary configuration $\vec{s}$ at constant $\tilde{\mu}_B$ and $\tilde{\mu}_{\mathrm{Va}}$. For a fixed binary configuration $\vec{s}$, it is convenient to introduce

a vacancy partition function defined as

$$z_{\mathrm{vac}}\left(\vec{s}\right)=\sum_{\vec{q}(\vec{s})}e^{-\beta\Delta\Omega(\vec{q}(\vec{s}))} \tag{17}$$

The sum in Eq. 17 extends over all configurations with at least one vacancy derived from the binary configuration $\vec{s}$.

It will prove useful to write the ternary partition function, Eq. 15, in terms of the binary partition function

$$\tilde{Z}=\sum_{\vec{s}}e^{-\beta\Omega(\vec{s})} \tag{18}$$

as

$$Z=\tilde{Z}\left(1+\xi\right) \tag{19}$$

with

$$\xi=\sum_{\vec{s}}\frac{e^{-\beta\Omega(\vec{s})}}{\tilde{Z}}\cdot z_{\mathrm{vac}}\left(\vec{s}\right)=\left\langle z_{\mathrm{vac}}\left(\vec{s}\right)\right\rangle_{\mathrm{binary}} \tag{20}$$

being the average of the vacancy partition function taken over the binary ensemble.

D. Equilibrium vacancy concentration

The equilibrium number of vacancies is equal to the ensemble average of vacancies given by

$$\bar{N}_{\mathrm{Va}}=\frac{1}{Z}\sum_{\vec{p}}N_{\mathrm{Va}}\left(\vec{p}\right)\cdot e^{-\beta\Omega(\vec{p})} \tag{21}$$

where $N_{\mathrm{Va}}\left(\vec{p}\right)$ is the number of vacancies in configuration $\vec{p}$. The expression for the equilibrium number vacancies can be rewritten using Eq. 19 as

$$\bar{N}_{\mathrm{Va}}=\frac{1}{\left(1+\xi\right)}\sum_{\vec{s}}\frac{e^{-\beta\Omega(\vec{s})}}{\tilde{Z}}\left(\sum_{\vec{q}(\vec{s})}N_{\mathrm{Va}}\left(\vec{q}\left(\vec{s}\right)\right)e^{-\beta\Delta\Omega(\vec{q}(\vec{s}))}\right). \tag{22}$$

The expression in brackets is equivalent to the partial derivative of the vacancy partition function, Eq. 17, with respect to $\beta\tilde{\mu}_{\mathrm{Va}}$, i.e.

$$\frac{1}{\beta}\frac{\partial z_{\mathrm{vac}}\left(\vec{s}\right)}{\partial\tilde{\mu}_{\mathrm{Va}}}=\sum_{\vec{q}(\vec{s})}N_{\mathrm{Va}}\left(\vec{q}\left(\vec{s}\right)\right)e^{-\beta\Delta\Omega(\vec{q}(\vec{s}))} \tag{23}$$

Inserting Eq. 23 into Eq. 22, we can write the equilibrium number of vacancies as

$$\bar{N}_{\mathrm{Va}}=\frac{1}{\left(1+\xi\right)}\sum_{\vec{s}}\frac{e^{-\beta\Omega(\vec{s})}}{\tilde{Z}}\left(\frac{1}{\beta}\frac{\partial z_{\mathrm{vac}}\left(\vec{s}\right)}{\partial\tilde{\mu}_{\mathrm{Va}}}\right) \tag{24}$$

or, because the binary grand canonical energy, $\Omega\left(\vec{s}\right)$, and the binary partition function, $\tilde{Z}$, do not depend on $\tilde{\mu}_{\mathrm{Va}}$, we can write using Eq. 20

$$\bar{N}_{\mathrm{Va}}=\frac{1}{\beta\left(1+\xi\right)}\frac{\partial\xi}{\partial\tilde{\mu}_{\mathrm{Va}}}. \tag{25}$$

No approximations have been made up to this point. Equation 25 shows that the equilibrium vacancy concentration should be accessible with a binary Monte Carlo simulation provided that the vacancy partition function, Eq. 17, can be evaluated in each binary configuration. The number of ternary vacancy configurations, $\vec{q}(\vec{s})$, for each binary configuration, $\vec{s}$, is unfortunately too large to be explicitly enumerated. However, if the equilibrium vacancy concentration is very low and the size of the crystal in the Monte Carlo cell is not too large, then microstates with two or more vacancies can be neglected in the vacancy partition function, Eq. 17, and we can approximate the vacancy partition function as

$$z_{\mathrm{vac}}\approx z'_{\mathrm{vac}}\left(\vec{s}\right)=\sum_{\vec{q}(\vec{s})'}e^{-\beta\Delta\Omega\left(\vec{q}(\vec{s})'\right)}, \tag{26}$$

where the sum now extends only over microstates containing one vacancy. This approximation is similar to that of a low temperature expansion. Within this approximation,

$$\frac{1}{\beta}\frac{\partial z'_{\mathrm{vac}}\left(\vec{s}\right)}{\partial\tilde{\mu}_{\mathrm{Va}}}=z'_{\mathrm{vac}}\left(\vec{s}\right), \tag{27}$$

allowing us to rewrite the expression for the equilibrium number of vacancies, Eq. 25, as

$$\bar{N}_{\mathrm{Va}}\approx\frac{\xi'}{\left(1+\xi'\right)}, \tag{28}$$

where

$$\xi'=\left\langle z'_{\mathrm{vac}}\left(\vec{s}\right)\right\rangle_{\mathrm{binary}}. \tag{29}$$

The approximate vacancy partition function, $z'_{\mathrm{vac}}\left(\vec{s}\right)$, can be readily evaluated in a binary Monte Carlo simulation.

The equilibrium vacancy concentration is defined as

$$x_{\mathrm{Va}} = \frac{\bar{N}_{\mathrm{Va}}}{M} \approx \frac{\xi'}{M\,(1+\xi')}. \tag{30}$$

This expression makes it possible to calculate the equilibrium vacancy concentration in a binary alloy with an arbitrary degree of disorder using a binary grand canonical Monte Carlo simulation. For each binary configuration sampled in the simulation, it is then necessary to calculate the grand canonical energy change of replacing each B atom at a time (or A, but not both) with a vacancy such that the vacancy partition function can be approximated using Eq. 26. The binary ensemble average of the vacancy partition function then yields ξ', Eq. 29, which is then to be inserted into Eq. 30. We emphasize that Eq. 30 is only valid if the equilibrium vacancy concentration is very dilute.

III. RESULTS

As an application of this approach, we study the thermodynamics of vacancies in hcp based Ti-Al binary alloys. The hcp crystal is a thermodynamically stable phase in the Ti-Al system for Al concentrations between 0 to 0.35, forming an hcp based solid solution at Ti rich concentrations and an ordered compound with stoichiometry around Ti_3Al. The hcp derived Ti_3Al compound has the DO_{19} ordering ($2\times2\times1$ supercell of the hcp unit cell) and is shown in Figure 2. The solubility of Al in the hcp based Ti-Al solid solution, commonly referred to as α, is large, reaching values above $x_{\mathrm{Al}} = 0.25$ at 1170°C[37]. The DO_{19} ordered phase, referred to as α_2, is stable over a wide concentration range around the perfect stoichiometry of $x = 0.25$. The rich variety of long and short-range order as well as large degrees of off-stoichiometry make the Ti-Al binary alloy a useful model system to explore the effect of alloy concentration and degree of ordering on the equilibrium vacancy concentration.

A. First-principles parameterization of alloy Hamiltonian

We parameterized a cluster expansion by fitting the coefficients of a truncated form of Eq. 3 to reproduce the formation energies of different arrangements of Ti, Al, and dilute vacancies over the sites of the hcp crystal structure (Figure 3). The energies of these configurations were calculated with density functional theory (DFT) as implemented in the Vienna *ab initio* Simulation Package (VASP)[38–42]. We used the projector augmented wave (PAW) pseudopotential method to treat the interaction between valence and core electronic states. A $10\times10\times5$ k-point mesh, yielding a convergence to within 1.0 meV per atom, was used for the hcp primitive cell and scaled accordingly to achieve equivalent (or greater)

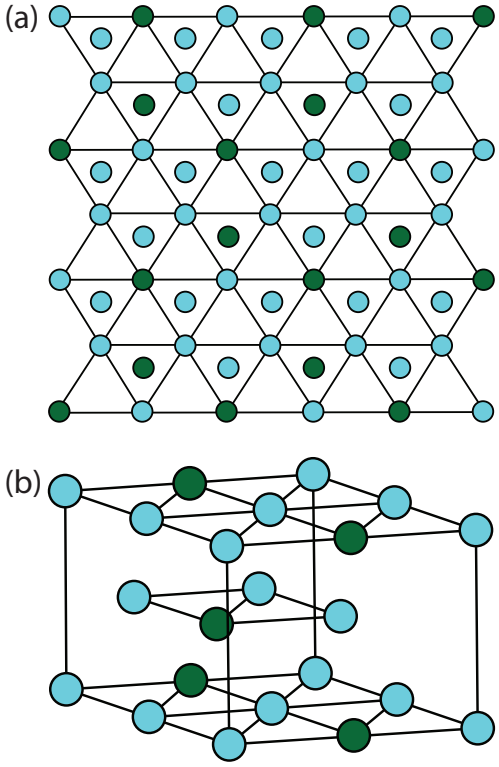

FIG. 2: Crystal structure schematics of the DO_{19} (α_2) ordered phase, including a 3D representation and a projection view down the c-axis.

k-point densities in supercells of the hcp primitive cell. The atomic positions, lattice parameters, and cell shape were allowed to relax fully. An energy cutoff of 450 eV was chosen for the plane wave basis set. These calculations were performed without the inclusion of spin polarization. We calculated the energies of over 600 binary

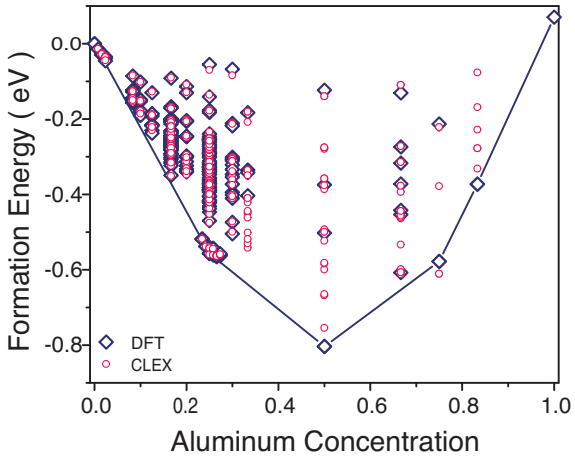

FIG. 3: DFT (blue diamonds) and cluster expansion predicted (pink circles) formation energies for the Ti-Al binary system as a function of Al concentration. Blue lines denote the convex hull and correspond to two-phase regions.

configurations by enumerating the symmetrically unique orderings of Ti and Al in all distinct supercells containing up to 6 hcp unit cells (up to 12 atoms per cell). In addition to these configurations, we also systematically enumerated dilute perturbations around the ground state configurations, which for the hcp based Ti-Al alloy are pure Ti and the ordered DO_{19} Ti_3Al phase. These dilute configurational perturbations were enumerated in a 128 atom, $4 \times 4 \times 4$ supercell of the hcp unit cell. For pure Ti, in the $4 \times 4 \times 4$ supercell, we calculated the energy of configurations generated by substituting one Ti for an Al, two Ti for a pair of Al, and three Ti for a triplet of Al. For the pair and triplet substitutions, we considered all symmetrically distinct Al-Al pairs up to the 8th nearest neighbor and a variety of symmetrically distinct Al-Al-Al triplets of increasing radius. Similar configurations were enumerated in a 128 atom supercell of DO_{19} (i.e. a $2 \times 2 \times 4$ supercell of the DO_{19} unit cell). Within this supercell, we calculated the energies of all anti-site defects (i.e. an Al on the Ti sublattice and a Ti on the Al sublattice), all symmetrically distinct pairs of anti-site defects up to the 8th nearest neighbor, and several symmetrically distinct triplets of anti-site defects.

The $4 \times 4 \times 4$ supercells were also used to enumerate different Al arrangements around a single vacancy. The choice of the $4 \times 4 \times 4$ supercell was motivated by a convergence analysis of the vacancy formation energy as a function of supercell size. We calculated the vacancy formation energy using supercells ranging from 42 to 162 atoms, allowing both the volume and lattice parameters to relax fully. We find that a 128 atom supercell yields a vacancy formation energy to within about 25 meV with respect to the largest 162 atom cell considered. Additionally, we find that smaller cells are noticeably less suitable as they differ by up to 50 meV from the most accurate value. This is shown in Fig. 4. Furthermore,

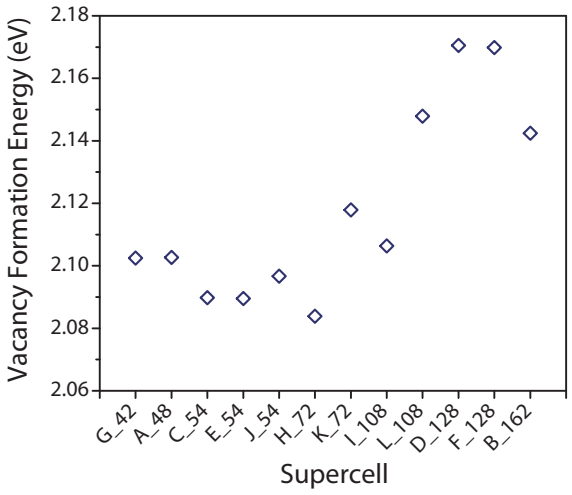

FIG. 4: Convergence test data for the vacancy formation energy in pure hcp Ti as a function of supercell size and shape.

using the 128 atom $4 \times 4 \times 4$ supercell of pure Ti, we calculated the energy of a single vacancy, of symmetrically distinct Al-vacancy pairs up to the 8th nearest neighbor, and of a variety of Al-Al-vacancy triplets. Similar configurations were enumerated in the 128 atom supercell of DO19. A single vacancy was placed on both the Al and Ti sublattices. We also enumerated symmetrically distinct vacancy-anti-site pairs up to the 8th nearest neighbor as well as several symmetrically distinct triplets containing two anti-sites and one vacancy. Configurations containing more than one vacancy were not considered due to the very dilute vacancy concentration in the alloy.

A large number of the more than 600 hcp based configurations considered here were found to be dynamically unstable and relaxed to fcc based orderings. This is consistent with the fact that the Ti-Al alloy forms fcc based compounds at aluminum concentrations of $x = 1/2$ and above. We did not include the energies of the dynamically unstable hcp-based orderings when fitting the coefficients of the cluster expansion. We identified configurations that relax to an fcc-based ordering based on the coordination number in the third and fourth nearest neighbor shells. The fcc crystal has 24 and 12 third and fourth nearest neighbors while the hcp crystal has 2 and 18. We only included the energies of configurations that can be mapped onto an hcp parent crystal if their nearest neighbor tables matched those of the primitive cell with a 0.2 Å tolerance on mapping any given atom into a shell. This leaves only 317 configurations, most of them Ti-rich.

The coefficients of the cluster expansion were determined by fitting to the fully relaxed DFT energies of 317 configurations using a genetic algorithm[43] followed by a depth-first-search algorithm to determine the optimal set of non-zero terms in the expansion[44] to minimize the cross validation score[45] and a penalty to minimize the number of coefficients in the expansion[46]. We use a number of different metrics to verify the predictive capability of the cluster expansion. The root mean square error between the original DFT energies and the corresponding energies predicted by the cluster expansion is 0.004 eV per primitive cell (containing two atoms). We also ensured that key trends in the first-principles data are reproduced by the cluster expansion. We verified, for example, that the energies of Al-Al and Al-Va pairs within a Ti hcp crystal have the same qualitative dependence on distance. The DFT calculations predict that the third nearest neighbor Al-Al pair in pure Ti is energetically more favorable than the first or second nearest neighbor pairs (Fig. 5b), while the energy varies negligibly beyond the fifth nearest neighbor distance. With Al-Va pairs, the energy spikes for the second NN, drops for the third, and spikes again for the fourth. These trends are all reproduced with the cluster expansion and shown in Fig. 5. One exception is the failure of the cluster expansion to capture the spike in the energy for a fifth-nearest neighbor Al-Al pair in pure Ti. Similar trends were reproduced between a pair of anti-site defects and a vacancy-anti-site defect in DO_{19}. We also ensured that the cluster

expansion predicts the correct ground states along the binary Ti-Al concentration axis between $x_{Al} = 0$ and 0.35 by calculating the energies of many additional configurations using the cluster expansion and by performing cooling runs in semi-grand canonical Monte Carlo simulations over a wide range of chemical potentials. The only ground states found to be stable on hcp at low Al concentrations are pure Ti and DO_{19} Ti_3Al.

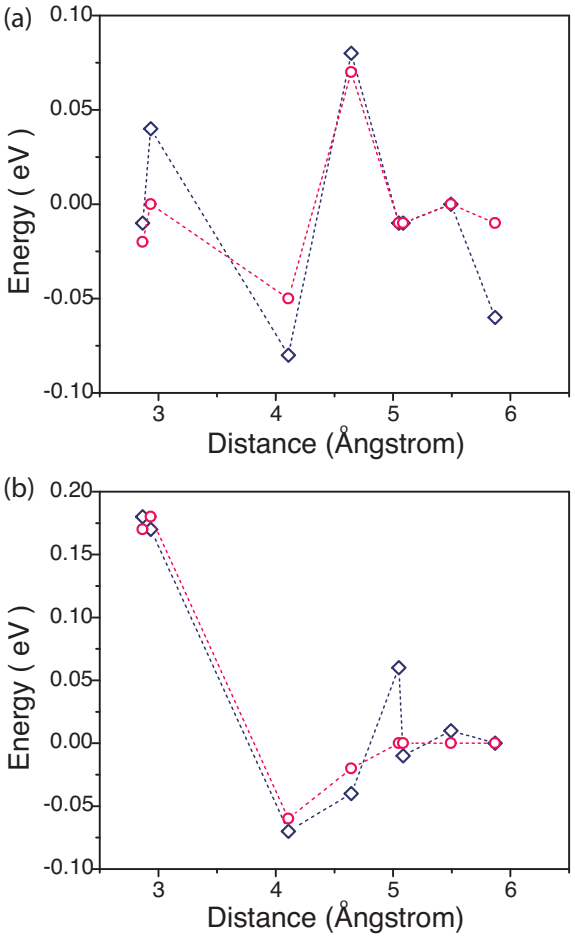

FIG. 5: Comparison of (a) Al-Va and (b) Al-Al pair cluster relative energies as calculated with DFT (blue diamonds) and predicted with the cluster expansion (pink circles).

As a final test of the quality of the cluster expansion, we sampled representative configurations within grand canonical Monte Carlo simulations at temperatures slightly above the order-disorder transition temperature of DO_{19} and compared their DFT energies with the energies predicted with the cluster expansion. The DFT-PBE energies of eight disordered configurations as sampled in a $4\times4\times4$ supercell of the primitive cell within Monte Carlo simulations were calculated with VASP. The rms between the DFT energies and those predicted by the cluster expansion for these eight configurations was 2 meV per hcp primitive unit cell. This low value, which is of the same order as the numerical accuracy of the direct DFT calculations, indicates that the cluster expansion has a predictive capability with first-principles accuracy.

B. Monte Carlo simulations

The cluster expansion was subjected to grand Canonical Monte Carlo simulations to predict a variety of thermodynamic properties, including the temperature concentration phase diagram of hcp based Ti-Al and the equilibrium vacancy concentration as a function of temperature and alloy concentration.

1. *Phase equilibrium*

Monte Carlo simulations were used to determine the binary temperature-concentration phase diagram. Since the vacancy concentration is very dilute in hcp Ti-Al, we performed binary semi-grand canonical Monte Carlo simulations (i.e. $x_{\rm Va} = 0$) to calculate bulk thermodynamic properties. Two-phase bounds separating the $Ti_{1-x}Al_x$ solid solution and DO_{19} Ti_3Al at low to intermediate temperatures were determined by minimizing over Gibbs free energies and grand canonical free energies as obtained with integration techniques of Monte Carlo calculated averages[33,44]. The two-phase bounds at high temperature were determined by tracking discontinuities in the concentration versus temperature curves obtained with heating and cooling grand canonical Monte Carlo simulations. At high temperature, there is very little hysteresis between heating and cooling runs. Figure 6 shows the resulting phase diagram for Ti-rich hcp Ti-Al. The DO_{19} Ti_3Al ordered phase, also referred to as α_2, is predicted to be stable up to approximately 1970 K (about 1700°C) and is stable over a wide concentration range. A wide two-phase coexistence region separates DO_{19} from a Ti-rich solid solution, α, while a narrower two-phase region separates DO_{19} from a high Al concentration hcp solid solution. At low temperature, DO_{19} can coexist with an fcc based ordering having TiAl stoichiometry. We did not consider phase stability between the hcp and fcc parent crystal structures. The lines in the phase diagram show the dependence of the average concentration x_{Al} on temperature T at constant $\tilde{\mu}_{\rm Al} = \mu_{\rm Al} - \mu_{\rm Ti}$ (i.e. iso-chemical potential lines). Figure 7 shows several binary Gibbs free energy curves ($g(x_{\rm Al})$ with $x_{\rm Va} = 0$) as calculated at different temperatures. The reference states of the free energies shown in Fig. 7 are pure hcp Ti and fcc Al. These free energies were obtained by integrating $\tilde{\mu}_{\rm Al}$ as a function of alloy concentration $x_{\rm Al}$ according to

$$g\left(x_{\rm Al}\right) = g\left(x_{\rm Al}^{\rm ref}\right) + \int_{x_{\rm Al}^{\rm ref}}^{x_{\rm Al}} \tilde{\mu}_{\rm Al} dx_{\rm Al} \qquad (31)$$

where $g\left(x_{\rm Al}^{\rm ref}\right)$ is the Gibbs free energy at a reference concentration, $x_{\rm Al}^{\rm ref}$, and the relation between $\tilde{\mu}_{\rm Al}$ and $x_{\rm Al}$ is calculated with binary semi-grand canonical Monte Carlo simulations ($x_{\rm Va} = 0$). As the reference concentration

for the free energy of the Ti-rich solid solution, we used $x_{\rm Al}^{\rm ref} = 0$ where $g\left(x_{\rm Al}^{\rm ref}\right) = 0$ is the formation energy of pure Ti (the configurational entropy is zero at $x_{\rm Al}^{\rm ref} = 0$). For the free energy of DO_{19}, we used a value for $x_{\rm Al}^{\rm ref}$ within the α_2 stability domain and determined the reference Gibbs free energy $g\left(x_{\rm Al}^{\rm ref}\right)$ by integrating the grand canonical free energy, $\phi = g - \tilde{\mu}_{\rm Al} x_{\rm Al}$, at constant $\tilde{\mu}_{\rm Al}$ as a function of temperature using[33]

$$\beta\phi\left(\tilde{\mu}_{\rm Al}, T\right) = \beta_{\rm ref}\phi\left(\tilde{\mu}_{\rm Al}, T_{\rm ref}\right) + \int_{\beta_{\rm ref}}^{\beta} \omega d\beta, \qquad (32)$$

where $\omega = e - \tilde{\mu}_{\rm Al} x_{\rm Al}$ is the average grand canonical energy calculated with the Monte Carlo simulations. As reference for the above integral, we used the ground state grand canonical energy of DO_{19} at low temperature (i.e. $\phi\left(\tilde{\mu}_{\rm ref}, T_{\rm ref}\right) = \omega_{DO_{19}}$).

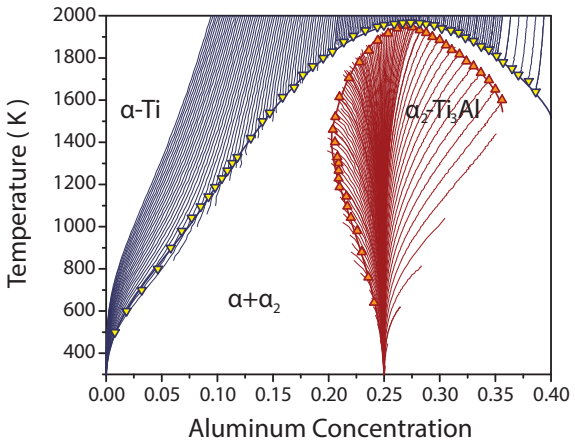

FIG. 6: Calculated temperature-concentration phase diagram for the Ti-Al binary system. Triangles represent points along the predicted phase boundary. Blue (cooling) and red (heating) lines are lines of constant chemical potential.

The Gibbs free energy, in addition to enabling the calculation of the equilibrium phase diagram is also needed to determine the values of $\tilde{\mu}_{\rm Va}$ corresponding to an equilibrium vacancy concentration (i.e. $\mu_{\rm Va} = 0$) according to Eq. 13. Because the vacancy concentration in the Ti-Al alloy is exceedingly low (about 10^{-17} to 10^{-6}), we can use the Gibbs free energy of the binary alloy in the absence of vacancies and neglect $x_{\rm Va}$ in Eq. 13. The resulting expression, $\tilde{\mu}_{\rm Va} = g(x_{\rm Al}) - x_{\rm Al}\tilde{\mu}_{\rm Al}$ then yields a relation between $\tilde{\mu}_{\rm Va}$ and $\tilde{\mu}_{\rm Al}$ consistent with an equilibrium vacancy concentration. Figure 8 (a and b) shows $\tilde{\mu}_{\rm Al}$ and $\tilde{\mu}_{\rm Va}$ as a function of alloy concentration calculated in this way. Figure 8c shows the relation between $\tilde{\mu}_{\rm Va}$ and $\tilde{\mu}_{\rm Al}$.

The exchange chemical potentials $\tilde{\mu}_{\rm Al}$ and $\tilde{\mu}_{\rm Va}$ of Figure 8 appear in the expression for the semi-grand canonical energy, Eq. 12. The Al exchange chemical potential, $\tilde{\mu}_{\rm Al}$, of Figure 8 increases with alloy concentration. The plateau (coinciding with a discontinuity in concentration) in $\tilde{\mu}_{\rm Al}$ as a function of alloy concentration (Fig.8a)

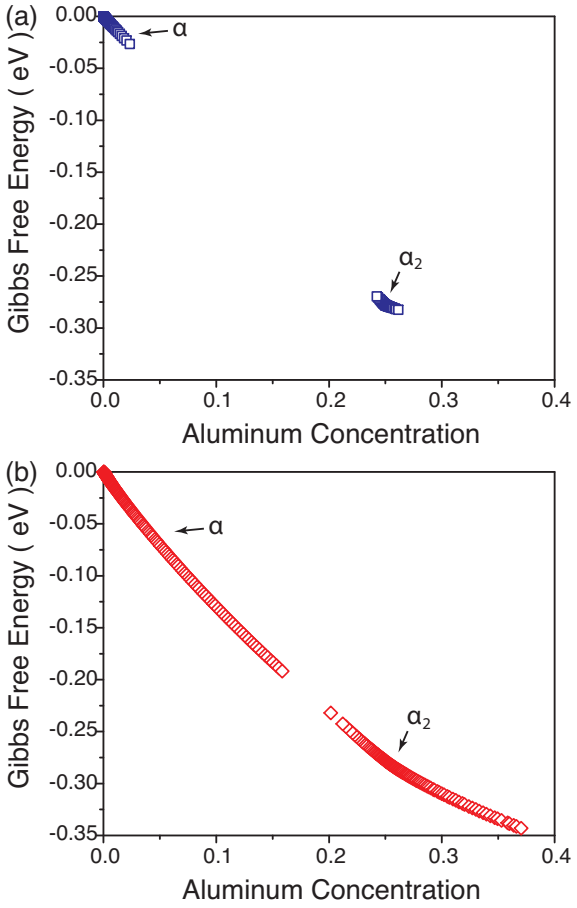

FIG. 7: Gibbs free energy curves for the hcp based Ti-Al binary at different temperatures: (a) 600 K (blue squares) and (b) 1600 K (red diamonds). The free energies are calculated using pure hcp Ti and fcc Al as references.

corresponds to the two-phase region separating the Ti rich solid solution and the DO_{19} ordered phase. The vacancy exchange chemical potential, $\tilde{\mu}_{\rm Va}$, when vacancies are in equilibrium, is equal to $-\mu_{\rm Ti}$, which using Eq. 6 and Eq. 10 can be shown to be related to the semi-grand canonical free energy (per crystal site) according to $\mu_{\rm Ti} = \phi = g - x_{\rm Al}\tilde{\mu}_{\rm Al} - x_{\rm Va}\tilde{\mu}_{\rm Va}$. The vacancy exchange chemical potential, $\tilde{\mu}_{\rm Va}$, also increases with alloy concentration. Both $\tilde{\mu}_{\rm Al}$ and $\tilde{\mu}_{\rm Va}$ increase very steeply at the stoichiometric Ti_3Al concentration due to the energetic preference for DO_{19} ordering and the energy penalty of anti-site defects that are needed when deviating from stoichiometry.

2. *Equilibrium vacancy concentration and the effect of order*

The large vacancy formation energy of approximately 2.15 eV in pure hcp Ti (Fig. 4) suggests that the equilibrium vacancy concentration will be very low in dilute hcp Ti-Al solid solutions. In addition to being ther-

mal defects, vacancies can also serve as structural defects in ordered compounds to accommodate deviations from perfect stoichiometry. While anti-site defects are commonly the dominant defect in many off-stoichiometric intermetallic compounds, compounds such as B2-NiAl can achieve substantial deviations from perfect stoichiometry through the introduction of very large concentrations of vacancies on one of the sublattices. The dominant point defects in a particular compound can be assessed by comparing defect formation energies defined as differences in the grand canonical energy of the compound with and without the point defect[4]. We find, using point defect energies calculated in 128 atom supercells, that the defect formation energies for vacancies are substantially larger than that for forming anti-site defects (by 1 to 2 eV) in the chemical potential interval stabilizing DO_{19} Ti_3Al. This indicates that anti-site defects accommodate off-stoichiometry in DO_{19} Ti_3Al (i.e. Al on the Ti sublattice or Ti on the Al sublattice) and that the concentration of anti-site defects are much higher than the equilibrium vacancy concentration. This is consistent with a previous analysis of point defects in DO_{19} Ti_3Al using point defect energies calculated with embedded atom interatomic potentials[57].

We calculated the equilibrium vacancy concentration at finite temperature within grand canonical Monte Carlo simulations applied to the ternary cluster expansion by explicitly sampling microstates in the full Ti-Al-Va ternary and by using the coarse-grained binary Monte Carlo algorithm introduced in Sec. II D. We used the relation between $\tilde{\mu}_{\rm Al}$ and $\tilde{\mu}_{\rm Va}$ of Figure 8 in the Monte Carlo simulations to ensure a path corresponding to an equilibrium vacancy concentration consistent with $\mu_{\rm Va} = 0$. Figure 9 compares the equilibrium vacancy concentrations at 1600 K as calculated with both approaches. The agreement between the full ternary Monte Carlo simulations and the coarse grained binary Monte Carlo simulations is very good. In the full ternary simulations, 6 to 12 million Monte Carlo passes were required (a Monte Carlo pass is the number of attempted site occupant exchanges per site) to attain well-averaged vacancy concentrations. The coarse-grained binary Monte Carlo required only of the order of several thousand Monte Carlo passes to achieve the same quality in the average vacancy concentration. Figure 10 shows the calculated equilibrium vacancy concentrations at several temperatures. Only the coarse-grained binary Monte Carlo algorithm was viable at the lower temperatures.

The calculated equilibrium vacancy concentration has a strong dependence on the alloy concentration, especially at lower temperatures. At both 600 K and 1100 K, the vacancy concentration varies by almost two orders of magnitude with alloy concentration. At all temperatures, the equilibrium vacancy concentration decreases with increasing Al concentration in the solid solution. It drops further when passing through the two-phase region from the solid solution to DO_{19}. Within DO_{19}, the equilibrium vacancy concentration decreases until the Al concentration reaches $x = 0.25$, then increases abruptly at $x = 0.25$, and finally levels off above $x = 0.25$. At 600 K, for example, the vacancy concentration increases by almost two orders of magnitude over a very narrow concentration range (about 0.01) around $x = 0.25$.

The equilibrium vacancy concentration is affected by the availability of energetically favorable local environments. This is determined by the equilibrium degree of short and long-range order between Al and Ti. Figure 11 shows the average Al concentrations within successive neighboring shells surrounding a vacancy (Figure 11 a and c) and an Al atom (Figure 11 b and d) as a function of alloy concentration, calculated at 1600 K. If the alloy is completely random, all shell concentrations will equal the Al concentration of the alloy. Deviations from $x_{\rm Al}$ indicate short-range order in the solid solution and long-range order in DO_{19}.

Figure 11 c and d shows that there is some degree of short-range order between Al, even at temperatures as high as 1600 K in the solid solution. At $x = 0$, all of the shell concentrations are zero as there are no Al atoms present in pure α-Ti. In the DO_{19} at $x = 0.25$, however, the calculated shell concentrations around Al (Figure 11d) show a strong preference for Al occupancy in the 3rd, 4th, and 8th neighbor shells, which is consistent with the Al long-range ordering in this phase. Figure 11c shows some degree of short-range order around vacancies, with a clear tendency for vacancies to prefer local environments in which the fourth nearest neighbor has a lower than average Al concentration. The fourth nearest neighbor as shown in Figure 11a corresponds to a pair parallel to the c-axis of the hcp crystal structure that connects sites separated by one close-packed layer. As shown in Figure 5a, the energy of a 128 atom Ti super cell containing a fourth nearest neighbor vacancy-aluminum pair is substantially higher than that of other vacancy-aluminum pairs in the same Ti supercell. As a result, vacancies prefer sites that have a low average Al concentration in the fourth nearest neighbor shell. Figure 11b shows slightly more short-range order in the neighboring shells of Al in the solid solution than exists around vacancies. The short-range order that Al prefers in the solid solution is similar to that of DO_{19}, though not as pronounced. In DO_{19}, the average Al concentrations of neighboring shells around a vacancy indicate that the vacancy prefers the Ti sublattice to the Al sublattice.

IV. DISCUSSION

We have explored the role of alloy concentration and variations in the degree of short and long-range order on the equilibrium vacancy concentration in multi-component crystalline solids, using the binary hcp based Ti-Al alloy as an example. A multi-component solid at finite temperature can exhibit a range of short and long-range order. The hcp based Ti-Al alloy exhibits both a solid solution and a stable ordered phase at $x = 0.25$

with a substantial tolerance to deviations from this ideal stoichiometric concentration. Variations in temperature and concentration in this alloy therefore result in different degrees of short and long-range order.

Explicitly accounting for vacancies in a two-component solid turns it into a ternary problem. Here we have used a ternary cluster expansion expressed in terms of polynomials of occupation variables to describe the interactions among Al and between Al and vacancies in an otherwise Ti-rich hcp crystal. The equilibrium vacancy concentration is determined by setting the vacancy chemical potential equal to zero, which is equivalent to minimizing the free energy of the solid with respect to the number of vacancies, holding the number of other components of the solid constant. Because vacancies usually have very low equilibrium concentrations, direct sampling using ternary grand canonical Monte Carlo simulations becomes intractable, especially at low temperature. Exploiting the exceedingly low equilibrium vacancy concentrations of most solids, we have developed a coarse graining scheme combined with a low-temperature-like expansion to calculate equilibrium vacancy concentrations with Monte Carlo simulations applied to the binary alloy. This is achieved by integrating out all dilute vacancy configurations within a disordered binary solid to obtain a vacancy partition function for each explicitly sampled binary configuration. The approach is similar in spirit to that followed by Benedek et al[60] to predict the thermodynamics of dilute ternary alloying additions to a binary alloy. A comparison between predictions of the full ternary grand canonical Monte Carlo simulations that explicitly account for vacancies and the coarse-grained binary Monte Carlo at high temperatures demonstrates the validity of the approximations inherent to the coarse graining procedure. The approximations within the coarse grained algorithm become more accurate with decreasing temperature, where the errors incurred by neglecting microstates involving more than one vacancy at a time in a Monte Carlo sized cell become negligible.

To ensure that the equilibrium short-range order sampled in Monte Carlo simulations is representative of that predicted by density functional theory, we fit the ternary cluster expansion to a large (> 300) database of DFT energies of Ti-Al-vacancy orderings on hcp. Among the configurations used to parameterize the cluster expansion were symmetrically distinct arrangements of a large number of point, pair, and triplet Al and vacancy arrangements within a large supercell of pure Ti and within a supercell of DO_{19} Ti_3Al. We ensured that the cluster expansion accurately reproduces the trends in Al-Al and Al-vacancy pair energies in pure Ti as well as anti-site-anti-site and anti-site-vacancy pair energies in DO_{19}. A comparison with representative high temperature configurations sampled at high temperature with Monte Carlo simulations also demonstrated that the cluster expansion has a predictive capability that matches the numerical accuracy of direct DFT calculations. The calculated phase diagram using this cluster expansion is similar to previous predictions of the $\alpha + \alpha_2$ phase bounds and predicts a transition temperature around 1970 K (about 1700°C), a value that is close to that predicted by van de Walle and Asta[33].

The experimental order-disorder transformation temperature is unknown due to the transformation of hcp Ti-Al to bcc Ti-Al at temperatures where DO_{19} Ti_3Al is still stable[37]. While early assessments of the Ti-Al binary phase diagram depicted an order-disorder transition temperature below the transformation of hcp Ti-Al to bcc[47–49], more recent assessments have concluded that it occurs at temperatures above the hcp to bcc transition[37,50]. The two-phase bounds and order-disorder transition temperature of approximately 1700°C were calculated in the absence of coherency strains. Most experimental samples, however, consist of a coherent two-phase mixture of an hcp Ti-rich solid solution, α, and DO_{19} Ti_3Al, α_2[50,51]. Coherency strains introduce a free energy penalty that depresses transition temperatures and decreases the widths of two-phase bounds[51–53]. An additional complexity arises from the fact that hcp Ti is capable of dissolving very high concentrations of oxygen in its interstitial octahedral sites, reaching concentrations as high as $TiO_{1/2}$. Many of the hcp based Ti-Al alloys also contain non-negligible oxygen concentrations, which will have an important effect on the order-disorder transition temperature of DO_{19}. Only a limited number of studies have explored the role of oxygen in modifying the equilibrium phase bounds between α and α_2[54]. Furthermore, there is a likelihood that dissolved oxygen can couple with coherency strains, for example by relieving a portion of the coherency strain energy penalty of two-phase coexistence by redistributing between the two phases[51]. This further complicates a comparison of the calculated order-disorder transition temperature to experiment.

Our present study only accounts for configurational degrees of freedom and neglects vibrational excitations. Van de Walle[55] recently incorporated the effect of vibrations in calculating the Ti-rich hcp Ti-Al phase diagram using length transferable force constants (LDTFCs) and a cluster expansion for the coarse-grained vibrational free energies. This study showed that the inclusion of vibrational excitations substantially decreases the DO_{19} order-disorder transition temperature. In fact, within the LDTFC approximation, the inclusion of vibrations decreases the transition temperature to values that are even below the earliest experimental estimates of this temperature. As with the phase diagram, the role of vibrational excitations is also likely to be important in determining the equilibrium vacancy concentration. In fact, a recent study has demonstrated the crucial role of anharmonic contributions in determining the equilibrium vacancy concentration in pure Al and Cu[56]. The same cluster expansion approach as well as the coarse-grained Monte Carlo algorithm used here can be applied when accounting for vibrational excitations in addition to con-

figurational degrees of freedom.

The results presented here show that the equilibrium vacancy concentration can vary by several orders of magnitude over relatively small intervals of alloy concentration. In the absence of long-range order, the vacancy concentration is predicted to decrease with increasing Al concentration. In DO_{19} Ti_3Al, the vacancy prefers to occupy the Ti sublattice rather than the Al sublattice. This result is in qualitative agreement with predictions made with embedded atom interatomic potentials as implemented in a mean field framework[57]. A vacancy preference for the Ti sublattice of Ti_3Al causes the vacancy concentration to increase abruptly once the Al concentration increases above the stoichiometric value of $x = 0.25$. An increase in the Al concentration above a stoichiometric Ti_3Al can be achieved in two ways: (i) by adding energetically costly Al anti-site defects to the Ti sublattice and (ii) by adding energetically more costly, vacancies to the Ti sublattice. While the vacancy concentration increases above x=0.25, Al anti-site defects on the Ti sublattice dominate to accommodate off stoichiometry in DO_{19}. The increase in vacancy concentration with Al concentration in α_2 between $x = 0.22$ and $x = 0.35$ agrees qualitatively with the dependence of an effective vacancy formation energy with Al concentration as determined with positron lifetime measurements[36].

An accurate description of vacancy solute interactions is a crucial input for predictions of diffusion coefficients in multi-component solids[58,59]. Interdiffusion coefficients are to first order proportional to the vacancy concentration[21]. The interdiffusion coefficient will therefore be very sensitive to large variations in the equilibrium vacancy concentration as a function of alloy concentration. The preference of vacancies for the Ti sublattice of DO_{19} Ti_3Al[31] will have important consequences for diffusion in the ordered phase[57]. The Ti sublattice forms an interconnected network, linked by nearest neighbor pairs. Hence, vacancies on the Ti sublattice can freely diffuse through DO_{19} without introducing any more disorder. The correlation factor for vacancies will therefore be quite high. In contrast, when vacancies prefer the minority sublattice (such as the Al sublattice in DO_{19} or the Li sublattice of $L1_2$ Al_3Li), which do not form an interconnected network, they will generally be trapped as typical nearest neighbor vacancy-atom exchanges result in an increase in disorder. The vacancy correlation factor is then very low[58]. The results here in combination with a prediction of the relevant diffusion coefficients[21] are of value in Allen-Cahn and Cahn-Hilliard type approaches to study precipitation of DO_{19} in supersaturated hcp based Ti-Al solid solutions.

V. CONCLUSION

We have developed a coarse graining scheme to predict the equilibrium vacancy concentration in alloys exhibiting arbitrary degrees of long and short-range order. We have applied this approach to determine the dependence of the equilibrium vacancy concentration on temperature and alloy concentration in hcp based Ti-Al binary alloys. We used a ternary cluster expansion, parameterized with first-principles DFT energies, to describe the interactions among solute atoms and vacancies within grand canonical Monte Carlo simulations. In the hcp based Ti-Al sytem, we find a strong dependence of the equilibrium vacancy concentration on Al concentration and degree of long range order.

Acknowledgments

The authors are grateful for funding provided by the Office of Naval Research under Grant N00014-12-1-0013 (project manager William Mullins). Computational resources provided by the National Energy Research Scientific Computing Center (NERSC), supported by the Office of Science and U.S. Department of Energy, under Contract No. DE-AC02-05CH11231, are also greatly acknowledged. We thank John Allison, Brian Puchala and John Thomas for helpful discussions. Some of the figures in this work were generated using the VESTA software[61].

* avdv@engineering.ucsb.edu;

[1] C. Freysoldt, B. Grabowski, T. Hickel, J. Neugebauer, G. Kresse, A. Janotti, and C.G. Van de Walle, Rev. Mod. Phys. **86**, 253 (2014).
[2] S.B. Zhang, S.H. Wei, A. Zunger, and H. Katayama-Yoshida, Phys. Rev. B **57**, 9642 (1998).
[3] A.F. Kohan, G. Ceder, D. Morgan, and C.G. Van de Walle, Phys. Rev. B **61**, 15019 (2000).
[4] C. Woodward, M. Asta, G. Kresse, and J. Hafner, Phys. Rev. B **63**, 094103 (2001).
[5] S.B. Zhang, S.H. Wei, and A. Zunger, Phys. Rev. B **63**, 075205 (2001).
[6] C.G. Van de Walle and J. Neugebauer, Journal of Applied Physics **95**, 3851 (2004).
[7] A. Janotti and C.G. Van de Walle, Applied Physics Letters **87**, 122102 (2005).
[8] A. Janotti and C.G. Van de Walle, Phys. Rev. B **76**, 165202 (2007).
[9] T.M. Pollock and S. Tin, J. Propul. Power **22**, 361 (2006).
[10] T.M. Pollock, J. Dibbern, M. Tsunekane, J. Zhu, and A. Suzuki, JOM **62**, 58 (2010).
[11] G.J. Snyder and E.S. Toberer, Nature Materials **7**, 105 (2008).
[12] J. Androulakis, C.H. Lin, H.J. Kong, C. Uher, C.I. Wu, T. Hogan, B.A. Cook, T. Caillat, K.M. Paraskevopoulos, and M.G. Kanatzidis, Journal of the American Chemical Society **129**, 9780 (2007).
[13] H. Chi, H. Kim, J.C. Thomas, X.L. Su, S. Stackhouse,

M. Kaviany, A. Van der Ven, X.F. Tang, and C. Uher, Phys. Rev. B **86**, 195209 (2012).
[14] H. Kim, M. Kaviany, J.C. Thomas, A. Van der Ven, C. Uher, and B.L. Huang, Phys. Rev. Lett. **105**, 265901 (2010).
[15] Q. Xu and A. Van der Ven, Intermetallics **17**, 319 (2009).
[16] A. Van der Ven, J. Bhattacharya, and A.A. Belak, Acc. Chem. Res. **46**, 1216 (2013).
[17] A. Van der Ven, J.C. Thomas, Q. Xu, B. Swoboda, and D. Morgan, Phys. Rev. B **78**, 104306 (2008).
[18] J. Bhattacharya and A. Van der Ven, Phys. Rev. B **83**, 144302 (2011).
[19] J. Bhattacharya and A. Van der Ven, Phys. Rev. B **81**, 104304 (2010).
[20] A. Emly, E. Kioupakis, and A. Van der Ven, Chem. Mater. **25**, 4663 (2013).
[21] A. Van der Ven, H.C. Yu, G. Ceder, and K. Thornton, Progress in Materials Science **55**, 61 (2010).
[22] A.D. Smigelskas and E.O. Kirkendall, Transactions of the American Institute of Mining and Metallurgical Engineering **171**, 130 (1947).
[23] Y.D. Yin, R.M. Rioux, C.K. Erdonmez, S. Hughes, G.A. Somorjai, and A.P. Alivisatos, Science **304**, 711 (2004).
[24] A.G. Evans, D.R. Mumm, J.W. Hutchinson, G.H. Meier, and F.S. Pettit, Progress in Materials Science **46**, 505 (2001).
[25] T.M. Pollock, D.M. Lipkin, and K.J. Hemker, MRS Bulletin **37**, 923 (2012).
[26] J.M. Sanchez, F. Duscatelle, and D. Gratias, Physica A **128**, 334 (1984).
[27] D. De Fontaine, *Solid State Physics* (Academic Press, 1994).
[28] M. Asta, C. Wolverton, D. de Fontaine, and H. Dreysse, Phys. Rev. B **44**, 4907 (1991).
[29] J.M. Sanchez, Phys. Rev. B **81**, 224202 (2010).
[30] G. Inden and G. Kostorz, *Phase Tranformations in Materials* (Wiley-VCH, 2001).
[31] A. Van der Ven and G. Ceder, Phys. Rev. B **71**, 054102 (2005).
[32] C.H.P. Lupis, *Chemical Thermodynamics of Materials* (Prentice Hall, 1983).
[33] A. van de Walle and M. Asta, Modelling Simul. Mater. Sci. Eng. **10**, 521 (2002).
[34] D.R. Trinkle, M.D. Jones, R.G. Hennig, S.P. Rudin, R.C. Albers, and J.W. Wilkins, Physical Review B **73**, 094123 (2006).
[35] A.T. Raji, S. Scandolo, R. Mazzarello, S. Nsengiyumva, M. Harting, and D. T. Britton, Philosophical Magazine **89**, 1629 (2009).
[36] R. Wurschum, E.A. Kummerle, K. Badua-Gergen, A. Seeger, Chr. Herzig, and H.E. Schaefer, Journal of Applied Physics **80**, 724 (1996).
[37] J.C. Schuster and M. Palm, J. Phase Equilib. **27**, 255 (2006).
[38] G. Kresse and J. Furthmuller, Computational Materials Science **6**, 15 (1996).
[39] G. Kresse and D. Joubert, Phys. Rev. B **59**, 1758 (1999).
[40] G. Kresse and J. Furthmuller, Phys. Rev. B **54**, 11169 (1996).
[41] P.E. Blochl, Phys. Rev. B **50**, 17953 (1994).
[42] J.P. Perdew, K. Burke, and M. Ernzerhof, Phys. Rev. Lett. **77**, 3865 (1996).
[43] G.L.W. Hart, V. Blum, M.J. Walorski, and A. Zunger, Nature Materials **4**, 391 (2005).
[44] B. Puchala and A. Van der Ven, Phys. Rev. B **88**, 094108 (2013)
[45] A. van de Walle and G. Ceder, J. Phase Equilib. **23**, 391 (2002).
[46] J.C. Thomas and A. Van der Ven, Phys. Rev. B **88**, 214111 (2013).
[47] J.L. Murray, *Phase Diagrams of Binary Titanium Alloys* (ASM International, 1987).
[48] U.R. Kattner, J.C. Lin, and Y.A. Chang, Metallurgical Transactions A – Physical Metallurgy and Materials Science **23**, 2081 (1992).
[49] I. Ohnuma, Y. Fujita, H. Mitsui, K. Ishikawa, R. Kainuma, and K. Ishida, Acta Mater. **48**, 3113 (2000).
[50] R. Kainuma, M. Palm, and G. Inden, Intermetallics **2**, 321 (1994).
[51] J.Y. Huh, J.M. Howe, and W.C. Johnson, Acta Metall. Mater. **41**, 2577 (1993).
[52] P.W. Voorhees and W.C. Johnson, Solid State Physics **59**, 1 (2004).
[53] J.W. Cahn and F. Larche, Acta Metall. **32**, 1915 (1984).
[54] J.Y. Lim, C.J. McMahon, D.P. Pope, and J.C. Williams, Metall. Trans. **7A**, 139 (1976).
[55] A. Van de Walle, JOM **65**, 1523 (2013).
[56] A. Glensk, B. Grabowski, T. Hickel, and J. Neugebauer, Physical Review X **4**, 011018 (2014).
[57] Y. Mishin and Chr. Herzig, Acta Materialia **48**, 589 (2000).
[58] A. Van der Ven and G. Ceder, Phys. Rev. Lett. **94**, 045901 (2005).
[59] Q. Xu and A. Van der Ven, Phys. Rev. B **81**, 064303 (2010).
[60] R. Benedek and A. van de Walle and S. S. A. Gerstl and M. Asta and D.N. Seidman and C. Woodward, Phys. Rev. B **71**, 094201 (2005).
[61] K. Momma and F. Izumi, J. Appl. Crystallogr. **41**, 653 (2008).

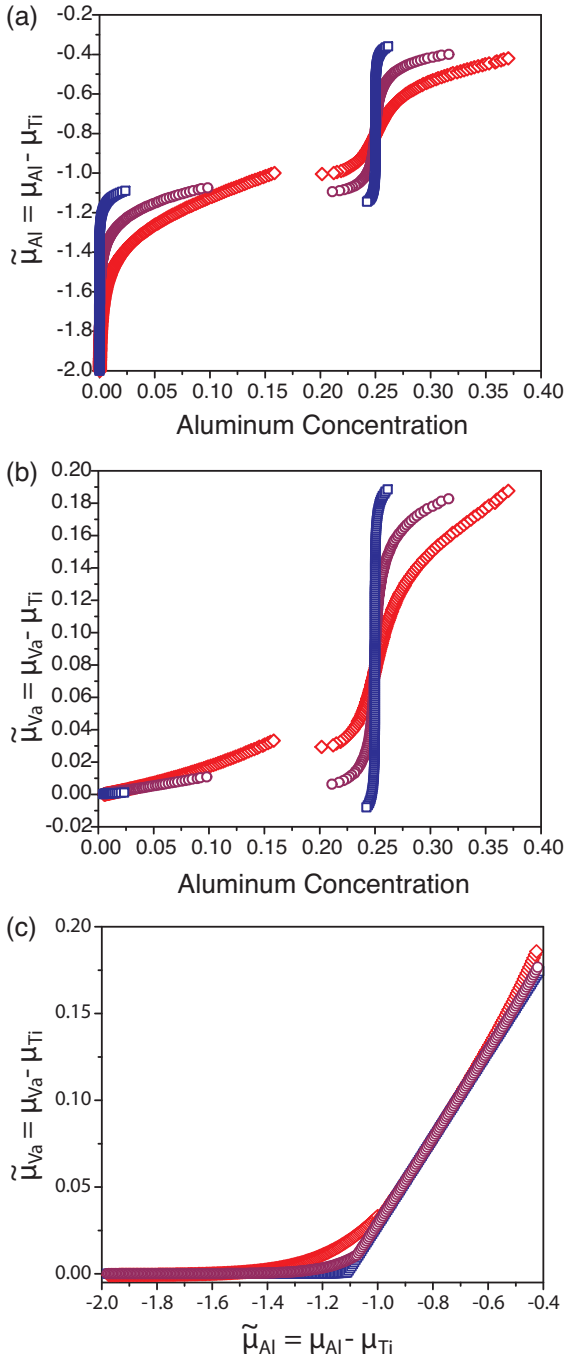

FIG. 8: The dependence of the exchange chemical potentials $\tilde{\mu}_{\mathrm{Al}}$ and $\tilde{\mu}_{\mathrm{Va}}$ on each other and on the Al concentration when $\mu_{\mathrm{Va}} = 0$, calculated using approximations that are valid when x_{Va} is very small. The data is shown at three different temperatures: 600 K (blue squares), 1100 K (purple circles), and 1600 K (red diamonds).

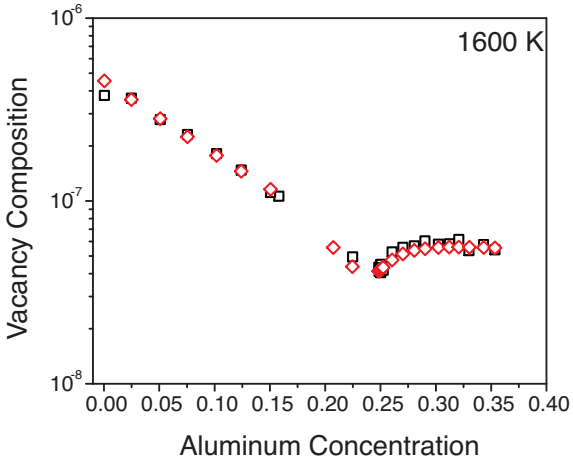

FIG. 9: Comparison of vacancy concentration as a function of Al concentration obtained by the Coarse Grained Monte Carlo method (red diamonds) and the full ternary Monte Carlo simulations (black squares) at 1600 K.

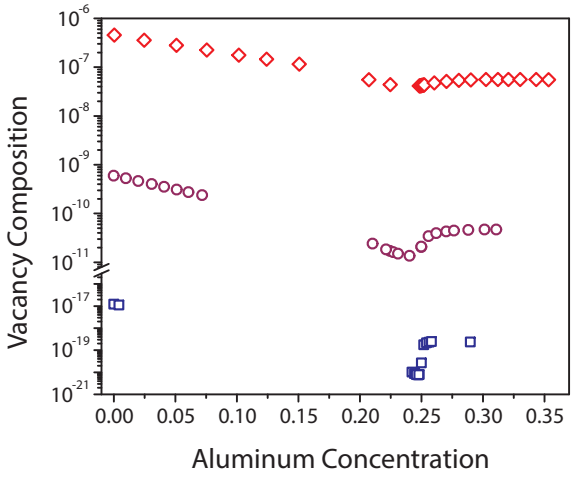

FIG. 10: Vacancy concentration as a function of aluminum concentration at different temperatures: 600 K (blue squares), 1100 K (purple circles), and 1600 K (red diamonds).

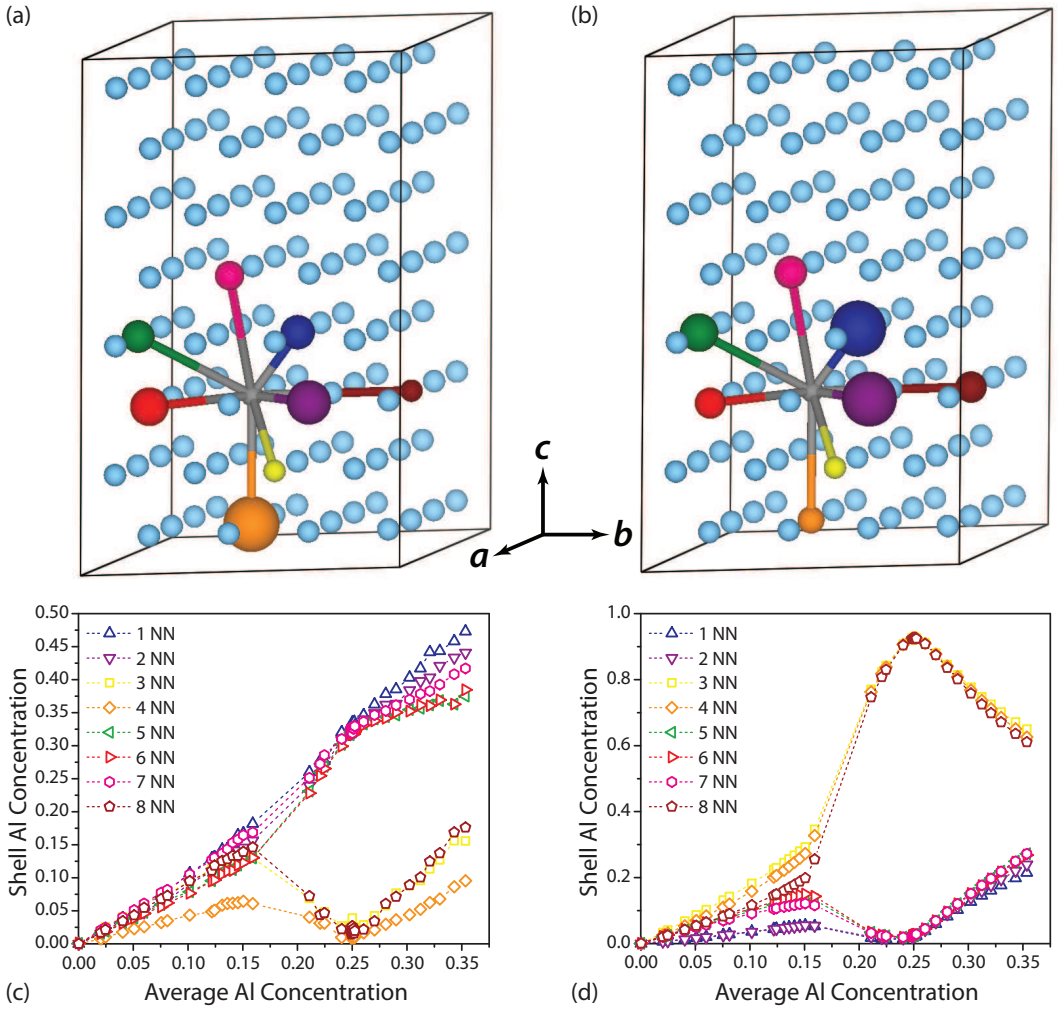

FIG. 11: Short-range order around a vacanacy and Al in the hcp Ti-Al system. Images (a) and (b) illustrate the collection of nearest neighbors 1 through 8 around a vacancy and aluminum, respectively, in hcp. The size of the balls correspond to the strength of the Va-Al and Al-Al interaction (absolute value) in pure titanium. In (c) and (d), the corresponding Al shell concentration around a vacancy and aluminum, respectively, is plotted as a function of the average Al concentration as calculated with the full ternary Monte Carlo simulations at 1600 K. The colors in all images consistently correspond to a specific nearest neighbor shell, as detailed in the plot legends (e.g. orange is always the 4th nearest neighbor).